Marine Geology 403 (2018) 179–190

Contents lists available at ScienceDirect

Marine Geology

journal homepage: www.elsevier.com/locate/margo

Differentiating the effects of advection and resuspension on suspended sediment concentrations in a turbid estuary

Yuan Li[a], Jianjun Jia[b], Qingguang Zhu[c], Peng Cheng[d], Shu Gao[b], Ya Ping Wang[a,b,*]

[a] Ministry of Education Key Laboratory for Coast and Island Development, Nanjing University, Nanjing 210093, China
[b] State Key Laboratory of Estuarine and Coastal Research, East China Normal University, Shanghai 200062, China
[c] Department of Environmental Sciences, University of Virginia, Charlottesville 22904, USA
[d] State Key Laboratory of Marine Environment Science, College of Ocean and Earth Sciences, Xiamen University, Xiamen, Fujian Province 361102, China

ARTICLE INFO

Editor: E. Anthony

Keywords:
Suspended sediment
Advection
Resuspension
Box model
Settling velocity
Changjiang Estuary

ABSTRACT

Suspended sediment concentration (SSC) has a significant impact on the estuarine environment and its morphological evolution. At any given location, the temporal variability of depth-averaged SSC is due to a combination of two processes: horizontal advection and local resuspension. In this study, we investigated the sediment dynamics at three anchored monitoring stations close to the maximum turbidity zone of the Changjiang Estuary, and developed a box model to differentiate the effects of advection and resuspension. Further, settling velocities were estimated using the ADV Reynolds flux method, excluding the advection SSC component. We found that predicted changes in advection- and resuspension-induced SSCs were consistent with the bottom shear stress and accretion/erosion observations. The combination of observed bed accretion/erosion changes and the predicted advection-induced SSCs indicates that the advective transport of suspended sediment is an important process in accelerating persistent erosion at the monitoring stations. Although SSC variations due to advection and resuspension are of similar magnitudes, our model results indicate that if resuspension dominates, the resuspension-induced component can reach up to twice the magnitude of the advection-induced component. We conclude that the box model is a valuable tool for evaluating subaqueous delta accretion/erosion in response to sediment reduction caused by upstream dam construction and climate change.

1. Introduction

Estuarine environments are affected by a combination of terrestrial, riverine, and marine processes. Here the characteristics of water flow dynamics and sediment transport processes have profound impacts on the estuarine morphology and ecosystem. As indicators of both flow dynamics and sediment transport processes, fine-grained sediments in estuarine waters play a significant role in shaping the seabed morphology, absorbing organic matter, and determining water clarity, and consequently affect the health of estuarine ecosystems and influence human activities (e.g., navigation and fisheries management) (Dyer, 1997).

The suspended sediment concentration (SSC) is an important variable when fine-grained sediment dynamics are considered. At any given location, the variation in SSC consists of horizontally advected and locally resuspended components (Krivtsov et al., 2008; Weeks et al., 1993). Now it is relatively easy to obtain, by measurements, time series data of SSC at a fixed location or through the entire water column; however, decoupling these data into the components that represent contributions by localized sediment resuspension and horizontal advection is still difficult because the characteristics of specific suspended sediment particles cannot be easily measured *in situ* (Bass et al., 2002; Hill et al., 2003; Hout et al., 2017; Jago et al., 2006). Moreover, because the erodibility of fine-grained sediment is influenced by multiple parameters, such as tidal currents, wind waves, storm events, and wave–current interactions, the impact of resuspension is difficult to predict (Kalnejais et al., 2007). To date, several approaches have been used to distinguish the advection and resuspension components of SSC. For instance, the relationships between SSC and both wave-induced shear stress and current flow have been used to investigate the principal mechanisms associated with high SSCs in specific estuaries (Cloern et al., 1989; Schoellhamer, 1995; Valipour et al., 2017), and vertical SSC profiles are used to predict the fate of suspended sediment (Bass et al., 2002; Li et al., 2016). Using the latter approach, Mitchell et al. (2017) reported that time-dependent SSC profiles covering a complete tidal cycle can help identify the arrival of an advective mobile “plug” of suspended sediment.

Numerical model has the potential to better differentiate the

* Corresponding author at: Ministry of Education Key Laboratory for Coast and Island Development, Nanjing University, Nanjing 210093, China.
E-mail address: ypwang@nju.edu.cn (Y.P. Wang).

https://doi.org/10.1016/j.margeo.2018.06.001
Received 28 November 2017; Received in revised form 4 June 2018; Accepted 7 June 2018
Available online 08 June 2018
0025-3227/ © 2018 Elsevier B.V. All rights reserved.

horizontal advection and local resuspension process of suspended sediment. Hamblin (1989) proposed a "two-box" model to study the horizontal transport and vertical diffusion of sediment and salt in the upper St. Lawrence Estuary (Canada). In the Irish Sea, a conceptual model established by Weeks et al. (1993) suggested that SSC variations associated with the M2 tide were caused primarily by advection, whereas those associated with the M4 tide were caused mainly by local sediment resuspension in marine environments dominated by the M2 tidal current. Hill et al. (2003) presented a 1-D Lagrangian particle-tracking model, incorporating the advection of a linear "background" concentration gradient, which was applied to the Dover Straits and Mersey Estuary (UK), to decouple the observed SSC time-series into background and resuspension components. Although such model-based studies have revealed the controlling factors for SSC variation, problems remain in terms of the quantitative separation of advection and resuspension components.

From a sediment dynamics viewpoint, settling velocity (w_s) represents an additional primary characteristic of fine suspended sediment and is a key to model the transport of fine-grained sediment (Shi et al., 2003). Shi et al. (2003) and Shao et al. (2010) estimated the settling velocity of suspended sediment in the Changjiang Estuary, China, by using the Rouse equation, assuming that w_s was a constant throughout the water column. Fugate and Friedrichs (2002) proposed the Reynolds flux method, which derives the settling velocity from Acoustic Doppler Velocimeter (ADV) signals; this functioning of ADV to measure both sediment concentration and settling velocity has been widely used (Voulgaris and Meyers, 2004; Friedrichs et al., 2008; Kawanisi and Shiozaki, 2008; Cartwright et al., 2013; Wang et al., 2013). However, the ADV method is unsuitable for areas where advection is significant, because it assumes that the horizontal gradient of SSC is negligible (Maa and Kwon, 2007). Therefore, a more comprehensive and reliable method is needed to differentiate the advection and resuspension effects.

In this contribution, we developed a box model that decomposes observed SSC time series to derive the horizontal advection and local resuspension components. We also suggested approaches to assess the model's validity. Furthermore, we attempted to determine the settling velocity based on the resuspension information obtained from the analysis.

2. Study area

Our study area is located outside the South Passage of the Changjiang Estuary (Fig. 1), a mesotidal estuary with a mean tidal range of 2.66 m and a maximum of 4.62 m at the river mouth (Shen et al., 2003). The multi-year average wind speed is 3.5–4.5 m s^{-1}, with maximum speeds reaching 36.0 m s^{-1} (Yang et al., 2008). Controlled by the monsoon climate, southeasterly winds prevail in summer whereas northwesterly winds dominate in winter (Yang et al., 2008). 67% of the sediment discharged from the Changjiang Estuary is finer than 50 μm and 95% is finer than 100 μm (Yang et al., 2001).

Changjiang is the largest river system in China. After the completion of the Three Gorges Dam, the average water and sediment discharges recorded at Datong (the nearest hydrological station to the Changjiang Estuary; Fig. 1a) were approximately 838 km^3 yr^{-1} and 145 Mt yr^{-1}, respectively (Yang et al., 2015). Sediment dispersal and accumulation in the Changjiang Estuary are controlled by the combined effects of tidal currents, waves and estuarine circulations (Sternberg et al., 1985; Su and Wang, 1986). Characterized by an SSC higher than the upstream and seaward areas, an estuarine turbidity maximum (ETM) is developed at the river mouth (Fig. 1b). The Changjiang ETM is remarkable not only for its high SSCs, but also for the high wash-load content (Li and Zhang, 1998).

3. Methods

3.1. Data collection

Tidal cycle measurements were carried out at three mounted monitoring stations (A, B, and C, Fig. 1b), located outside the South Passage of the Changjiang Estuary on July 2–3, 2016. The distance between stations A and C was 33.4 km. The mean water depths were 10.5, 13.8, and 21.7 m at stations A, B, and C, respectively. Southerly wind speeds reached 11–19 m s^{-1} and contributed to the generation of local waves with a maximum wave height of > 2 m.

Velocity profiles were measured using a downward-looking Acoustic Doppler Current Profiler (ADCP, 1200 kHz) at station A, and two upward-looking ADCPs (600 kHz) at stations B and C. At station A, the velocity profile ranged from 0.85 m below the sea surface to near the seabed, with a vertical resolution (bin size) of 0.2 m. At stations B and C, the profile range extended from approximately 2 m below the sea surface to the seabed, with a bin size of 0.5 m. The sampling

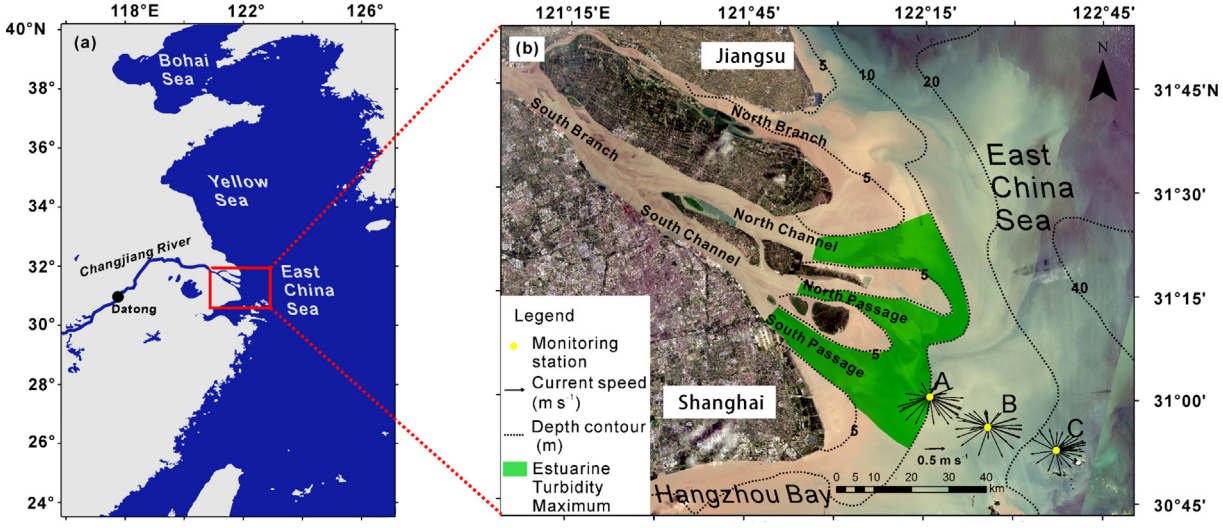

Fig. 1. Maps of the study area, showing (a) the location of the Changjiang Estuary, and (b) monitoring stations (yellow circles). Black arrows represent depth-averaged current speeds in m s^{-1}, measured hourly from 09:00 July 2 to 12:00 July 3, 2016 (UTC/GMT + 08:00). The zone of estuarine turbidity maximum in (b) is from Li and Zhang (1998). (For interpretation of the references to colour in this figure legend, the reader is referred to the web version of this article.)

frequency of the ADCPs was 1 Hz.

Water temperature, salinity, and turbidity profiles were collected every hour using optical backscatter sensors (OBS-3A, Campbell Scientific) at station A and two conductivity–temperature–depth loggers (CTD XR-620, RBR Ltd) equipped with turbidity sensors at stations B and C. The frequency of the OBS-3As and CTDs at the three stations was 1 Hz. Turbidity profiles were calibrated with water samples collected hourly from the water column, for which SSCs were obtained via filtration analysis (using 0.45 μm filters). Additionally, we used a grab sampler to collect seabed sediment samples at stations A and B; the grain size distributions were analyzed with a laser Malvern Mastersizer 2000 granulometer (range 0.02–2000 μm; duplicate measurement error < 3%).

Two bottom-mounted tripods were deployed at stations A and B. At station A, the tripod was equipped with two OBS-3As at 0.3 and 0.7 m, and one ADV (6 MHz Nortek Vector) positioned 0.3 m above the seabed. The tripod located at station B was equipped with two ADVs at 0.28 and 0.85 m above the bed; the lower ADV also recorded the distance between the ADV probe and the seabed. All the ADVs were set up in autonomous mode at a sampling frequency of 16 Hz in 10 min bursts (8192 samples in every 10 min).

3.2. Data processing and analysis

3.2.1. Estimate of suspended sediment concentration

The vertical SSC profiles for all the three stations were based on the laboratory-derived calibration curve that relates the OBS or CTD turbidity measurements (T; NTU) to the SSC (C; mg L^{-1}) of the water samples as follows:

$$C = \alpha \cdot T + K \tag{1}$$

where C is suspended sediment concentration, and α and K are coefficients determined by linear regression analysis. The calibration results show that SSC is significantly correlated with turbidity (Fig. 2a–c), demonstrating the reliability of turbidity-based SSC measurements.

For station B, the backscattered signal intensity of the ADV mounted 0.85 m above the seabed was converted to SSC (Wang et al., 2013). According to acoustic principles, the relationship between SSCs (C; mg L^{-1}) and the ADV acoustic intensity value (I_{ADV}; dB) can be expressed by (Thorne and Hanes, 2002):

$$\log_{10}(C) = \beta \cdot I_{ADV} + b \tag{2}$$

where β and b are coefficients determined by linear regression analysis (Fig. 2d). Our results indicate that SSCs can be predicted from I_{ADV} based on the calibration relationship. Thus, high-frequency SSC data were obtained from the time series of ADV acoustic intensity values.

The suspended sediment transport rate (q_s; kg m^{-1} s^{-1}) was calculated by (Dyer, 1986):

$$q_s = \int_0^h c(z)v(z)dz = \sum_{j=1}^{n} c_j v_j \Delta z \tag{3}$$

where h is the water depth; c_j and v_j are the SSC and current velocity in the j^{th} layer of the water column, respectively; and Δz is the thickness of the jth layer.

3.2.2. Box model for depth-averaged SSC signal treatment

To isolate the respective contributions of advection and resuspension, we developed a box model (Fig. 3), in which sediment input from the box boundaries constitutes the sole factor influencing advective SSC variability in the water column. Resuspension and settling were considered to be two internal processes capable of influencing the SSC within the box. Station B was located at the center of the box, and the SSC time series at this station represents the mean SSC for the box resulting from both horizontal advection and local resuspension processes. Thus, the resuspension component of SSC within the box system can be estimated using SSC time series measured at station B and advection-induced SSC values calculated through the box boundaries.

Fig. 3 depicts the box model covering the three monitoring stations. This box was 32.1 km long from east to west, and 9.3 km wide from north to south, with an average depth of 15.33 m. We define l as the length of the edge of the box. For example, l_{bc} is the length of the edge bc of the box (Fig. 3) and l_{bc} is equal to l_{ad}. Similarly, l_{bc_i} represents the length of the edge bc at the i^{th} hour, and l_{ad_i}, i.e. the water depth at A, was obtained from the hourly *in situ* observation; $l_{b'c'_i}$, the water depth of station C at the i^{th} hour, can also be obtained from the observational data. Thus, the volume of the box at the i^{th} hour (V_i; m^3) is:

$$V_i = \frac{1}{2}(l_{bc_i} + l_{b'c'i})l_{bb'}l_{ab} \tag{4}$$

At stations A or C, q_s can be decomposed into eastern and southern components. For instance, $q_{s(A)}$ can be decomposed into $q_{s(A,E)}$ and $q_{s(A,S)}$ (Fig. 3), representing the sediment transport rate at the western and northern boundaries of the box, respectively. Similarly, $q_{s(C,E)}$ and $q_{s(C,S)}$ of station C are the sediment transport rates on the eastern and southern boundaries, respectively. Ideally, there would be four monitoring stations located at the center of the edges aa′, bb′, ab, and a′ b′ of the box model. However, due to limitations in instrumentation and practical difficulties associated with *in situ* measurement, data from only three stations were available. The implications will be discussed on the validity and uncertainty associated with the box model in Sections 5.1 and 5.2.

The amount of suspended sediment (M_i; kg) transported into the box system from outside at the i^{th} hour is:

$$M_i = [(q_{s(A,E)} - q_{s(C,E)})l_{ab} + (q_{s(A,S)} - q_{s(C,S)})l_{aa'}]\cdot t \tag{5}$$

where t = 3600 s.

The SSC caused by advection processes at the i^{th} hour ($C_{(ad)i}$; kg m^{-3}) is:

$$C_{(ad)i} = C_0 + \sum_{j=0}^{i} \frac{M_j}{V_j} \tag{6}$$

where C_0 is the SSC at the 0^{th} hour.

Finally, the sediment resuspension and advection signals can be decoupled using:

$$C_m = C_{re} + C_{ad} \tag{7}$$

where C_m is the depth-averaged SSC (i.e., mean SSC) measured at station B and C_{re} is the resuspension-induced SSC component.

3.2.3. Estimate of sediment settling velocity using the box model output

The advection-induced SSC data obtained from the box model were used in conjunction with the ADV Reynolds flux method to calculate the settling velocities. Fugate and Friedrichs (2002) initially proposed the method. If the horizontal sediment advection is negligible, the burst-averaged settling velocity (w_s) can be estimated as:

$$w_s < C > = < w'C' > \tag{8}$$

where w' and C' are the vertical velocity fluctuation and the concentration fluctuation, respectively, estimated from the ADV sensor, the diamond brackets denote the burst-average, and C is the suspended sediment concentration. This method is applicable if advection is relatively weak.

However, the estimate by Eq. (8) will be biased towards low values by the presence of a non-settling "wash load" component related to advection. Cartwright et al. (2013) pointed out that sediment concentration (C) measured by ADV backscatter can be represented by the sum of a non-settling wash load component (C_{wash}) with a zero settling velocity and a settling component (C_{sett}) with a characteristic mean settling velocity. The balance in Eq. (8) then becomes $w_s < C_{sett} > = < w'C_{sett}' >$. As the non-settling wash load component is spread much more evenly in the water mass than the settling

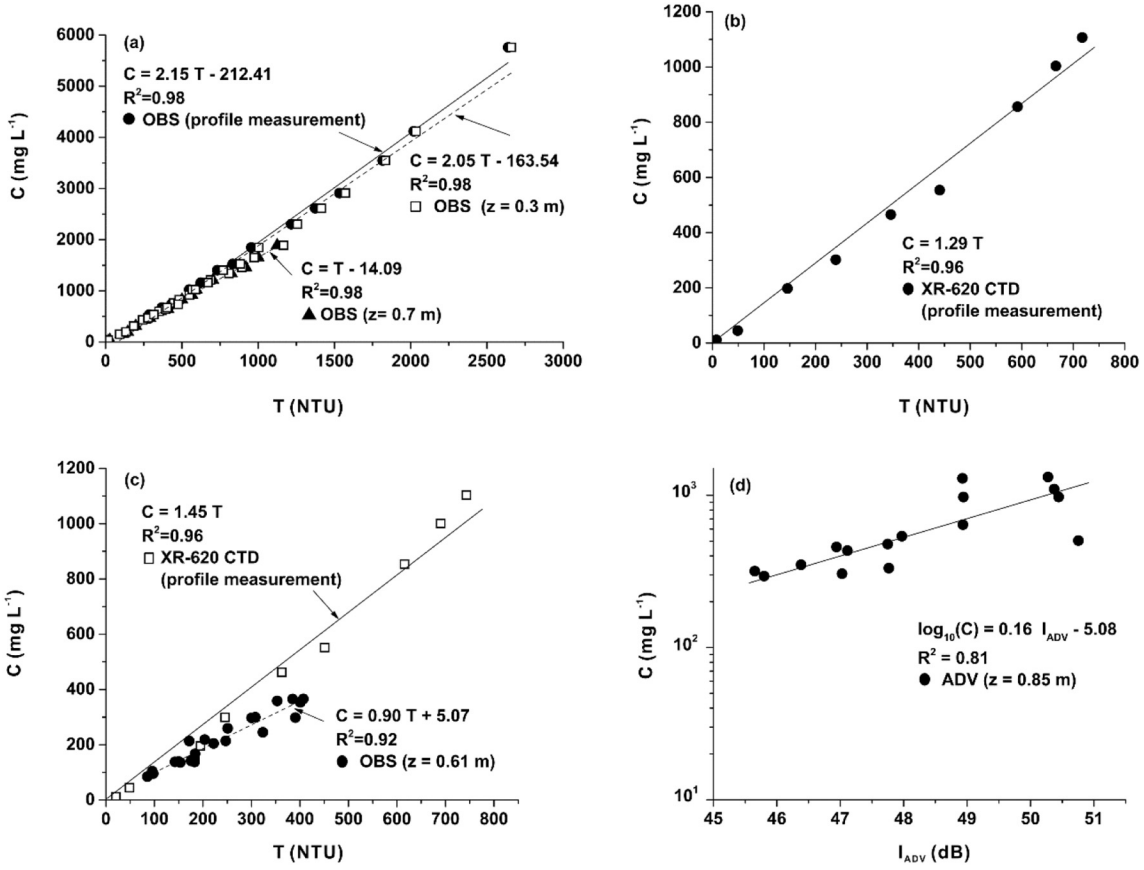

Fig. 2. Calibration curves used to convert (a, b, and c) optical turbidity (T; NTU) to SSC (C; mg L^{-1}) and (d) the acoustic signal to SSC. Values in (a), (b), and (c) represent calibration curves for stations A, B, and C, respectively. (d) includes the calibration equation used to convert the ADV-derived acoustic intensity values (I_{ADV}; dB), from 0.85 m above the bed, to SSC at station B.

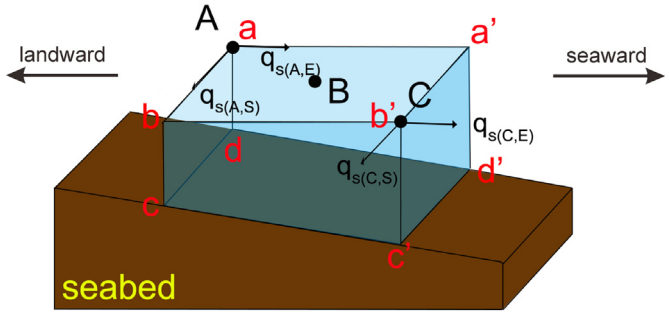

Fig. 3. Schematic diagram of the box model. Black dots marked A, B, and C represent the three monitoring stations in Fig. 1. Lower-case letters a–d and a′–d′ represent the eight vertices of the box. The terms $q_{s(A,E)}$ and $q_{s(A,S)}$ represent sediment transport rates towards the east and south, respectively, at station A, while $q_{s(C,E)}$ and $q_{s(C,S)}$ represent the sediment transport rates towards the east and south, respectively, at station C.

component, $C_{wash}' \ll C_{sett}'$, this expression can be re-written as:

$$w_s(<C> - C_{wash}) = <w'C'> \quad (9)$$

In this method, the C_{wash} value was represented by the minimum SSC observed near slack water suggested by Cartwright et al. (2013). We used w_{sw} to represent the settling velocity calculated by Eq. (9).

In the box model, the depth-averaged SSCs (C_m) are divided into an advection component (C_{ad}) and a resuspension component (C_{re}). The proportion of advection component (P_{ad}) can be calculated by:

$$P_{ad} = \frac{C_{ad}}{C_m} \quad (10)$$

The time series of P_{ad}, which in our box model has a time interval of 1 h, reveal the variability of the advection-induced component within the total SSC. Consequently, P_{ad} needs to be interpolated over the same time interval of the ADV burst (i.e., 10 min) prior to being used to separate the SSC derived from the ADV backscatter into the advection and resuspension components. Assuming that P_{ad} is applicable to every layer within the water column, the advected SSC component measured by ADV backscatter in the bottom layer (C_{ad_b}) becomes $C_{ad\_b} = C \times P_{ad}$. Thus, the constant value C_{wash} in Eq. (9) can be replaced by a more realistic value (C_{ad_b}) that varies with time:

$$w_s(<C> - C_{ad\_b}) = <w'C'> \quad (11)$$

Eq. (11) implies that the w_s value can be defined by the bottom layer measurements, and w_s estimated from this equation is represented by w_{sb}.

3.2.4. Estimates of bottom shear stress and bed-level change

The bottom shear stress (τ_c; N m^{-2}) was estimated using the Reynolds method. The instantaneous horizontal and vertical velocity can be represented by a time mean flow and a turbulent deviation (Dyer, 1997):

$$u = \overline{u} + u' \quad (12)$$

$$w = \overline{w} + w' \quad (13)$$

where $\overline{u}$ and $\overline{w}$ are the mean flows, and u' and w' are turbulent fluctuations.

The Reynolds stress can be estimated as follows:

$$\tau_c = \rho \cdot (-\overline{u'w'}) \quad (14)$$

where ρ is the density of seawater.

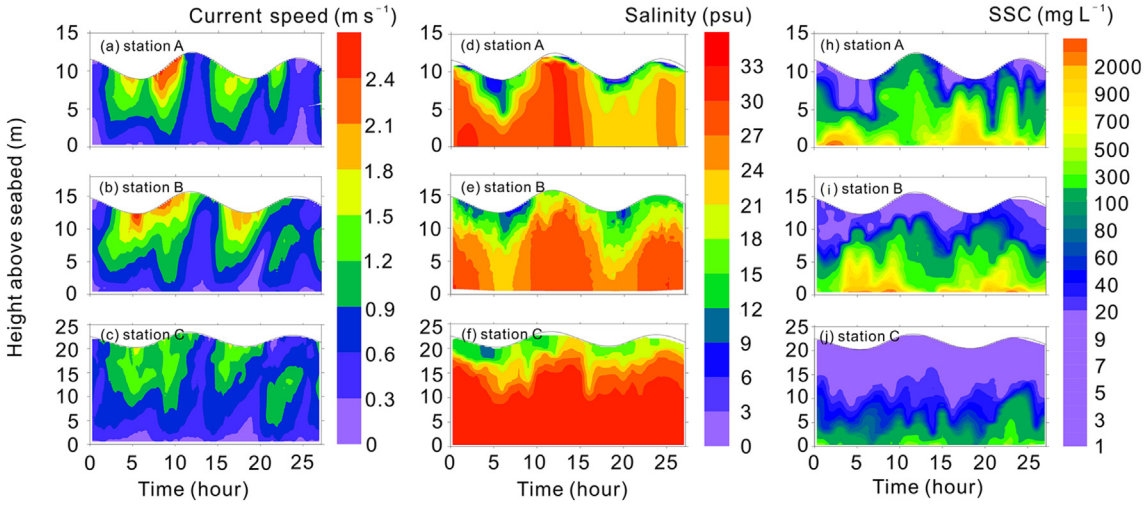

Fig. 4. Vertical and temporal variabilities in (a, b and c) current speed (m s^{-1}), (d, e and f) salinity (psu), and (h, i and j) SSC (mg L^{-1}) for the three stations.

The ADV can measure simultaneously the 3D turbulent-scale velocity and the relative temporal change in elevation (Salehi and Strom, 2012) if the probe elevation is < 0.5 m. This elevation change record contains a series of values noted at the same sampling frequency as the velocity record, and we averaged these values every 10 min. Here, the cumulative bed-level change (ΔZ) was obtained using the ADV installed 0.28 m above the bed. Thus, ΔZ_i (ΔZ at the ith hour) can be calculated from:

$$\Delta Z_i = D_i - D_1 \quad (15)$$

where D_i represents the ith averaged distance between the sensor and the bed.

4. Results

4.1. Temporal variability in hydrodynamics and sediment characteristics

Fig. 4 shows the hydrodynamic and sediment dynamic variations for one summer spring tide period. The depth-averaged current velocities at the three stations reveal that the tidal currents are rotatory in the study area, with a flood dominance pattern (Fig. 4a–c). At the first high tide of the observation period, a phase difference between current speed and water level was observed i.e. ~30 min after high water level at station A, and ~1 h after high water level at stations B and C. In the upper water column, the current velocity was not minimal at ebb slacks; the maximum surface current speeds at stations A, B, and C were 2.40, 2.25 and 1.60 m s^{-1}, respectively. At around 1.0 m above the bed, the minimum speeds decreased to 0.08 (station A), 0.08 (station B), and 0.02 (station C) m s^{-1}. Between hour 20 and hour 25, the current speeds at all three stations were smaller in the upper water column than at lower levels. Possible reasons for this pattern include wind direction, which was opposite to the flow direction, and momentum balance among barotropic, baroclinic pressure gradients and bottom friction (Cudaback and Jay, 2001; Helfrich, 1995; Stacey et al., 2001; Uncles, 2002).

The time series of salinity profiles (Fig. 4d–f) show different patterns. At station A, the salinity difference between the surface and bottom layers was small during the high water slack, indicating that vertical mixing was strong at that time. Five hours after the high water slack, stratification was enhanced by the river discharge. Salinity decreased with ebb tide, and rose with flood tide, indicating that station A was located in a region where river influence is relatively intense. At station B, the salinity distribution indicates that stratification was intensified during the ebb and weakened during the flood. Accordingly, the vertical salinity gradient was greatest at low tide, with the lowest salinity (6 psu) occurring in the surface layer and the highest (22 psu) near the bed. The salinity signal showed a clear tidal variability, which means that, compared with at station A, the influence of tides was larger at station B. For station C, stratification was the dominant feature of the surface water. Salinity remained high (> 33 psu) from the bed to approximately 10 m from the floor, indicating that river discharge affects only the uppermost part of the water column.

The values of SSCs are shown at a logarithmic scale (Fig. 4h–j) for better visualization. A distinct horizontal SSC gradient existed in the study area, whereby SSCs were higher near the river mouth and decreased gradually seaward. The influence of horizontal SSC gradient on the validity of the assumption made for the box model needs evaluation (for an uncertainty analysis, see Section 5.2). The SSC profiles also showed differences within the water column. At stations A and B, high concentrations occurred near the bed at high speed occasions, with peak values exceeding 3400 mg L^{-1}, an indication of sediment resuspension. At station C, SSC values were relatively low (< 200 mg L^{-1}) throughout most of the water column with the exception of the high water periods (up to 400 mg L^{-1} near the bed).

For the bottom sediment samples collected near the monitoring stations, the median grain size at stations A and B was 8.69 μm (6.85 ϕ) and 16.45 μm (5.93 ϕ), relatively. The grain size distributions were unimodal and the proportion of silt plus clay reached 96.4% and 86.6% at stations A and B, respectively (Fig. 5). Sediment containing > 10% by mass of fine-grained sediment (grain size finer than 63 μm or > 4 ϕ) should exhibit cohesive properties (Whitehouse et al., 2000). Such a high proportion of silt and clay would affect the erodibility of the seabed sediment, and make it more difficult to determine the accretion/erosion condition using critical shear stress calculation.

4.2. Time series of advection- and resuspension-induced SSC variations

The time series of advection-induced SSC (C_{ad}) and resuspension-induced SSC (C_{re}) were decoupled using the box model (Fig. 6), showing that the horizontal advection and locally resuspension processes were both strong. Positive C_{re} values indicates resuspension dominance, if C_{ad} is smaller than C_m, according to Eq. (7). In contrast, advection and accretion become the dominant processes if C_{ad} exceeds C_m. The values of C_{re} revealed that the bed was transferred from an accretion-dominant phase to a resuspension-dominant one at around hours 2–3, and returned to accretion-dominance at around hour 10.

The suspended sediment transport rates (q_s) at stations A, B, and C are shown in Fig. 7. When C_{re} (Fig. 6) was positive, the net transport rate at station B was greater than that during the period when C_{re} was negative, indicating that the resuspension process contributed to the

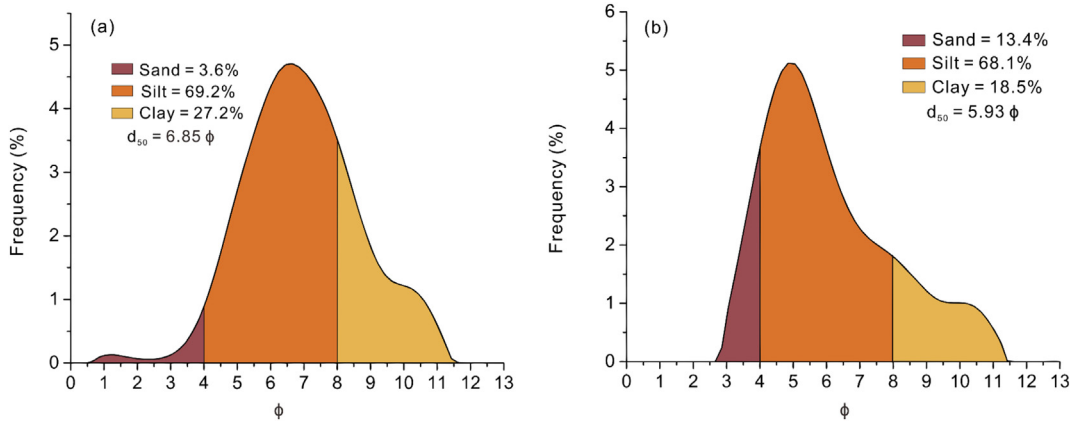

Fig. 5. Grain size distribution of bottom sediments sampled from (a) station A and (b) station B.

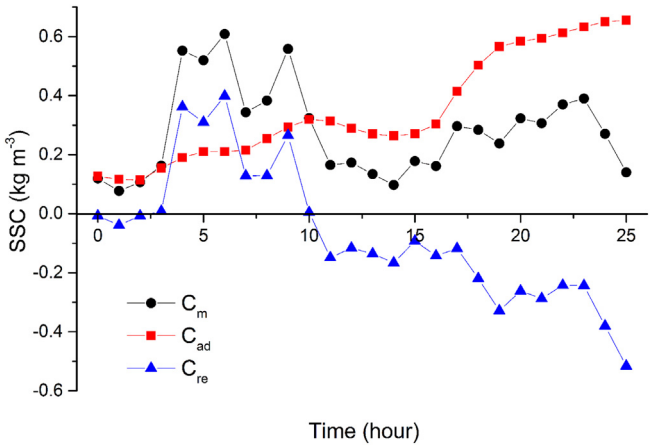

Fig. 6. Time series of C_m, C_{ad}, and C_{re} (kg m^{-3}). C_{ad} and C_{re} are horizontal advection and local resuspension components, respectively, determined by the box model.

Table 1
Net sediment transport at stations A–C during a 25–hour tidal cycle.

Station	Net sediment transport (kg m^{-1})	Net sediment transport direction (degree, azimuth)
A	55,292.76	163.5
B	37,483.28	255.6
C	16,336.13	351.9

suspended sediment transport. Net sediment transport during a 25–hour tidal cycle exhibited an overall decrease seaward (Table 1); this pattern should be considered in the box model (see below). At station A, sediment transport occurred primarily towards the east and south, and the magnitude of sediment transport was smaller during the flood tide than during the ebb tide. For station B, sediment transport was primarily towards the west and south, and the maximum net transport rate at this station exceeded those of the other two stations, reaching nearly 8 kg m^{-1} s^{-1}. At station C, sediment transport was predominantly towards the north and the transport rate was smaller than at the two other stations. The maximum sediment transport rate at this station (1.6 kg m^{-1} s^{-1}) occurred around hour 23.

The time series of bottom shear stress (τ_c) at station B (black line in

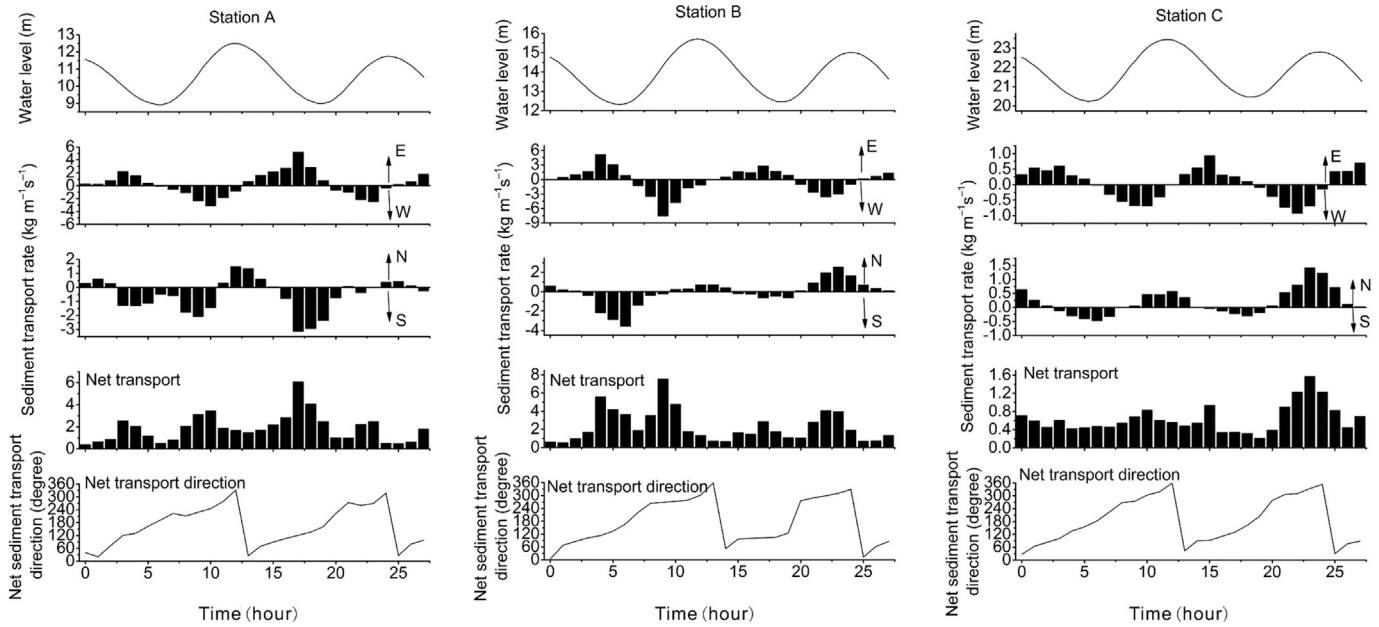

Fig. 7. Sediment transport rates at the three monitoring stations. Positive values indicate eastward and northward transport. Negative values indicate westward and southward transport.

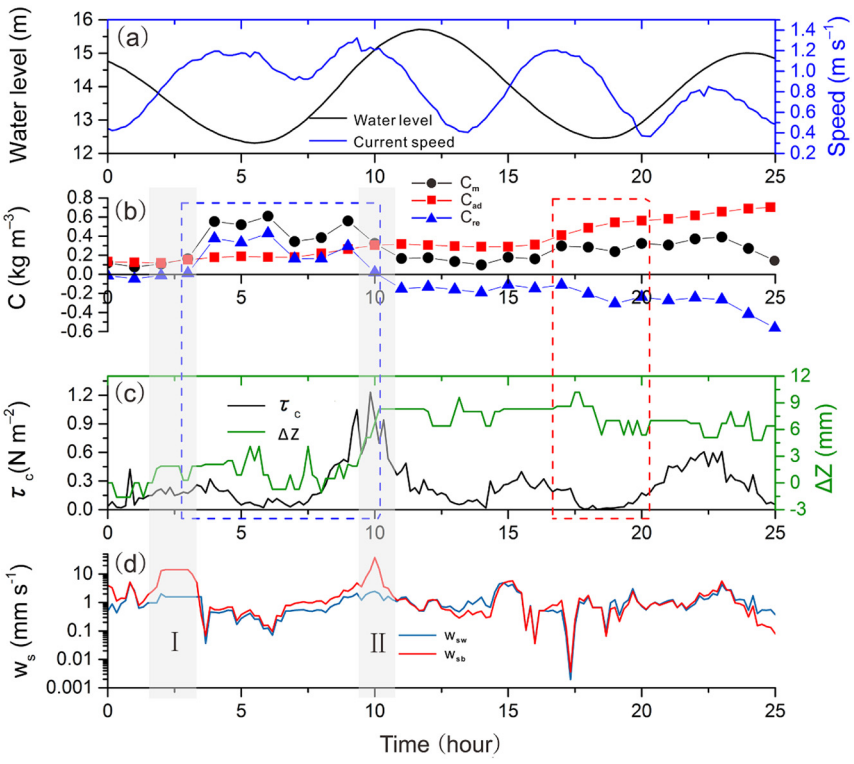

Fig. 8. Time series of (a) water level (m) and depth-averaged current speed (m s^{-1}), (b) C_{ad}, C_{re}, and C_m (kg m^{-3}), (c) shear stress (N m^{-2}) and cumulative bed-level changes (ΔZ; mm), and (d) settling velocity (w_s; mm s^{-1}) estimated from the ADV signal using the ADV Reynolds flux method at one ADV sensor level (0.85 m above the bed). Note: w_{sw} represents w_s estimated by introducing the wash load, and w_{sb} represents w_s estimated from the results of the box model (Eq. (11)). Cumulative bed-level change (ΔZ) represents the change in relative distance between the ADV probe and the seabed compared with the distance at the beginning of the observation period. Positive ΔZ values indicate that the distance between the ADV probe and seabed has increased relative to the original distance, and vice versa. The value of ΔZ increases with increasing distance between ADV probe and seabed. (For interpretation of the references to color in this figure, the reader is referred to the web version of this article.)

Fig. 8c) exhibits a significant increase from 0.1 to a maximum of 1.2 N m^{-2} between hours 7.5 and 10. Cumulative bed-level changes (ΔZ; mm) calculated from Eq. (15) are shown in Fig. 8c (green line). When τ_c increased from 0.1 to 1.2 N m^{-2}, there was a large concomitant increase in ΔZ of approximately 8 mm, after which ΔZ remained almost unchanged during the hour 10–18 period before decreasing to a sustained value of about 6 mm. Between hour 10 and hour 15 C_{ad} exceeded C_m (Fig. 8b), indicating that bed accretion occurred. However, ΔZ measured over the same period did not exhibit a sustained decrease, indicating that the ADV is incapable of measuring discrete elevation changes. Therefore, our study suggests that more accurate altimeter measurements are required to increase the accuracy of bed-level change estimates.

4.3. Variations of settling velocity

By using the Rouse equation to estimate w_s, one may concentrate on selected times, e.g., close to the maximum ebb when there is no stratification (Shao et al., 2010). However, factors including unsteady tidal flows, salinity stratification related to circulation processes, and varying w_s in the water column mean that the Rouse equation is not entirely appropriate for estimating w_s in estuarine environments. In the Changjiang Estuary, resuspension is mainly controlled by the alternative tidal current (Li and Zhang, 1998), and horizontal advection also plays a significant role in SSC variations (Fig. 8b). Jay et al. (2015) reported that time variations of horizontal transport are likely to change the balance between the vertical turbulent transport and sediment settling as assumed by Fugate and Friedrichs (2002).

The time series of advection-related SSC, derived from the box-model analysis, were used to calculate the settling velocity via the ADV Reynolds flux method. Time series of w_s estimated in this way, for station B, are shown in Fig. 8d, plotted using logarithmic coordinates. Values of w_{sw} were calculated using Eq. (9) and w_{sb} by Eq. (11). For much of the time, these two outputs were similar. However, there were two periods when w_{sb} was an order of magnitude greater than w_{sw} (i.e., two gray rectangles in Fig. 8, representing hours 2–3 and hour 10).

We defined the periods represented by the first and second gray rectangles as periods I and II, respectively (Fig. 8d). During period I, w_{sb} reached 16.7 mm s^{-1}, while during period II maximum w_{sb} was 45.6 mm s^{-1}. Both values appeared to be too high. However, when these two periods are neglected from the dataset, it is evident that for much of the observation period w_{sb} varied within the range 0.04–6.66 mm s^{-1}, with a mean value of 1.43 mm s^{-1}.

We note that during period I, C_{re} (Fig. 8b) underwent a transition from negative to positive values, indicating that sediment suspended in the seawater changed from a settling- to a resuspension-dominant phase. The opposite process occurred during period II. The abrupt increases in w_s measured during periods I and II may relate to the phase change in suspended sediment movement. For example, a considerable volume of sediment was eroded from the bed and transferred to the water column during period I. At this time, the newly eroded sediment might be flocculated, causing an abrupt increase in w_s. During period II, when suspended sediment transitioned from resuspension to settling, any bottom sediments that could potentially be mobilized under these hydrodynamic conditions had already been eroded. Moreover, the concomitant decrease in shear stress (Fig. 8c) precluded further erosion of the bed. Advection-derived suspended sediment began to accumulate rapidly, resulting in the high measured values of w_{sb}, and the difference between C_m and C_{ad} became small. The sudden increase in w_s during periods I and II indicates that an “intense settling event” may occur during the transition period from resuspension to deposition, or vice versa.

5. Discussions

5.1. Validity of the box model

Sediment resuspension in estuaries is affected by marine and riverine processes. Due to the limited timeframe (i.e. two tidal cycles), there is a concern about the accuracy of dividing the advection and resuspension effects, using the three station system and the idealized box. In the method adopted, the data measured at two marginal stations (A and C) were used to define status changes in the box, which is compared with the actual condition of the box (represented by the data

from station B).

A direct verification is given by a comparison between the calculated results and the measured data. The validity of the box model is demonstrated by the data shown in Fig. 8b and c. First, ΔZ increased by 3 mm in the first half of the period denoted by the blue dashed line in Fig. 8c, indicating that sediment erosion and resuspension were dominant at that time. Meanwhile, C_m was greater than C_{ad} (Fig. 8b), a pattern interpreted as the response of SSC to erosion, as outlined before. Then, at the end of the first half period indicated by the blue dashed line, τ_c increased rapidly to a peak value of 1.2 N m^{-2}, causing relatively intense erosion (i.e. ΔZ showing a significant increase of approximately 8 mm). The concurrent increase in the difference between C_m and C_{ad} (Fig. 8b) is consistent with the measure of ΔZ. After this rapid increase in ΔZ, τ_c declined and C_m became smaller than C_{ad}. From hour 10 onwards, C_{re} was negative (Fig. 8b), indicating that accretion was the dominant process. Throughout this period, ΔZ decreased by about 3 mm (red dashed line in Fig. 8c) and the difference between C_m and C_{ad} increased, indicating a simultaneous increase in sediment accumulation. Thus, the synchronized change between SSC and ΔZ provides a general assessment of the box model accuracy.

In future studies, it would be interesting to test whether or not this box model can be made applicable to larger or smaller areas. This can be achieved by estimating the net gain of sediment for single hypothetical box incorporating marginal stations. It should be noted that if the area of the hypothetical system is expanded, then additional factors influencing sediment transport (e.g., sediment sources located far from the marginal stations) must be considered. For larger scale systems, we speculate that a greater number of marginal stations and longer observation periods would lead to better estimates of C_{ad}.

5.2. Uncertainty along the box boundary

In Eq. (5), sediment transport across the box model boundaries is regarded as constant, an assumption that might lead to inaccuracies due to the presence of horizontal coast–sea SSC gradients. Within our study area, SSC decreases in the seaward direction (Fig. 4h–j), suggesting that the rate of southward suspended-sediment transport might exhibit a gradient along the northern and southern boundaries. Hence, for the applicability of the box model, the influence of horizontal gradient in the suspended sediment transport rate should be evaluated, which is discussed below.

If a distance between the two monitoring stations in the outer Changjiang Estuary is small, i.e. < 10 km, the longitudinal sediment transport rate can be regarded as a constant (e.g. Xie et al., 2017); in this case the horizontal gradient of the transport rate can be neglected. In our box system, the length of the west-east boundaries was 9.3 km, whereas the length of the north-south boundaries was 32.1 km. It is necessary, therefore, to include the horizontal gradient of sediment transport rate at the box boundaries.

To investigate the sediment transport gradients, we used the calibrated numerical model (Xing et al., 2012) to simulate the hydrodynamics and SSC patterns in the Changjiang Estuary. Details of the numerical model setup and validation are presented in Appendix A. To evaluate the horizontal gradient of the suspended sediment transport rate (HGSR) along the box system boundaries, we exported depth-averaged SSC ($\overline{C}$) and velocity ($\overline{V}$) data from ten additional stations, i.e., A1, A2, and A3 for the northern boundary; C1, C2, and C3 for the southern boundary; A4 and A5 for the western boundary; and C4 and C5 for the eastern boundary (Fig. 9a), using the numerical model.

The numerical model predicted suspended sediment transport rates (R$_{mp}$; kg m^{-1} s^{-1}) for each station can be represented as:

$$\mathrm{R}_{mp} = \overline{V}\,\overline{C}\cdot\mathrm{H} \tag{16}$$

where H represents the water depth. Consequently, the HGSR (G; kg m^{-2} s^{-1}) between A and Ai (i = 1, 2, 3, 4, 5) is

$$G(Ai) = \frac{\mathrm{R}_{mp}(Ai) - \mathrm{R}_{mp}(A1)}{\Delta X(Ai)} \tag{17}$$

where $\Delta X(Ai)$ is the distance between A and Ai. The HGSR values between C and Ci (i = 1, 2, 3, 4, 5) can be calculated in the same way. The time series of the horizontal gradient of the suspended sediment transport rates are shown in Fig. 10.

Using the HGSR values calculated from the model outputs and the suspended sediment transport rates measured at stations A and C, we were then able to derive a numerical model extrapolated suspended sediment transport rate (R_{me}; kg m^{-1} s^{-1}). For the northern and western boundaries, this is:

$$R_{me}(\mathrm{Ai}) = O(A) + G(Ai) \times \Delta X(Ai) \tag{18}$$

where $O(A)$ is the observed suspended sediment transport rate at station A. For the southern and eastern boundaries, the equation is

$$R_{me}(\mathrm{Ci}) = O(C) + G(Ci) \times \Delta X(Ci) \tag{19}$$

In the calculation of sediment fluxes, the transport rate for each station is decomposed into eastern and southern components. Each station located on the boundary represents a certain width of the boundary (see N0, N1, N2, and N3 on the northern boundary; S0, S1, S2, and S3 on the southern boundary; W1 and W2 on the western boundary; and E1 and E2 on the eastern boundary; Fig. 9a). Thus, the gradient-engaged suspended sediment flux (Q; kg s^{-1}) is:

$$\mathrm{Q}_S(\mathrm{N}) = \mathrm{O}_S(\mathrm{A}) \times \mathrm{N0} + \sum_{i=1}^{3} R_{me,S}(\mathrm{Ai}) \times \mathrm{Ni} \tag{20}$$

$$\mathrm{Q}_S(\mathrm{S}) = \mathrm{O}_S(\mathrm{C}) \times \mathrm{N0} + \sum_{i=1}^{3} R_{me,S}(\mathrm{Ci}) \times \mathrm{Si} \tag{21}$$

$$\mathrm{Q}_E(\mathrm{W}) = R_{me,E}(\mathrm{A4}) \times \mathrm{W1} + R_{me,E}(\mathrm{A5}) \times \mathrm{W2} \tag{22}$$

$$\mathrm{Q}_E(\mathrm{E}) = R_{me,E}(\mathrm{C4}) \times \mathrm{E1} + R_{me,E}(\mathrm{C5}) \times \mathrm{E2} \tag{23}$$

where subscripts $_S$ and $_E$ represent the southward and eastward suspended sediment transport components, respectively, and the parenthesized N, S, W, and E on the left-hand-side of each equation represent the northern, southern, western, and eastern boundaries, respectively. For example, Eq. (20) represents the southward suspended sediment flux for the northern boundary.

Consequently, in the gradient-engaged method, Eq. (5) is rewritten as:

$$M_i = [(\mathrm{Q}_E(\mathrm{W}) - \mathrm{Q}_E(\mathrm{E})) + (\mathrm{Q}_S(\mathrm{N}) - \mathrm{Q}_S(\mathrm{S}))]\cdot t \tag{24}$$

where t = 600 s. By combining Eqs. (24), (6) and (7), we obtained an additional value for the separation of resuspension and advection signals. We defined this output as the MIKE21 numerical-model-corrected result. Thus, C_{ad} estimated in this manner is defined as C_{ad_mc}, whereas C_{re} calculated via C_{ad_mc} is C_{re_mc}.

The original and MIKE21 numerical-model-corrected box model results show that the HGSR along the box boundaries have relatively small influence on the box model results (Fig. 11a, b). This finding indicates that the horizontal gradient of the suspended sediment transport rate (Fig. 10) is not contradictory to the results of the box model. Furthermore, this outcome suggests that the arrangement of the monitoring stations is reasonable in terms of the spatial scale of the present study (i.e., ~10 km).

However, if the space scale is further enlarged (e.g., to 10^2 km), the technique to separate advection and resuspension affects presented here may not be applicable. As a test, we used the same MIKE21 model, with the original box model being enlarged by four times (Fig. 9b). Base on the same procedures outlined above, the results with and without the consideration of transport gradient are shown in Fig. 11c, d. It illustrates that in this case the error becomes large. This observation also shows that, for the areas where horizontal gradient of suspended sediment transport rate is similar to those obtained in this paper (Fig. 10),

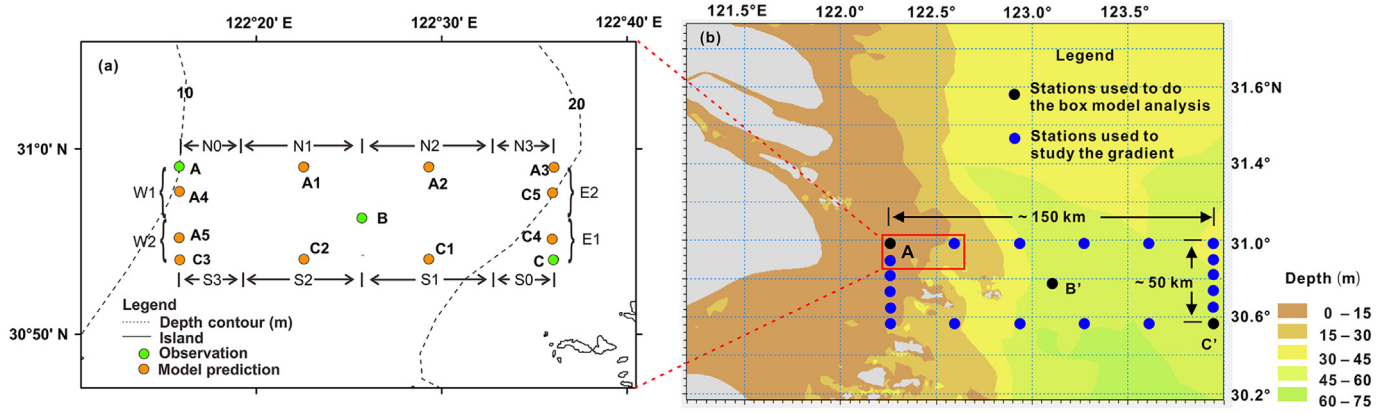

Fig. 9. MIKE21 numerical model predicted stations for box model calculations at the space scale of (a) ~10 km, and (b) ~10^2 km.

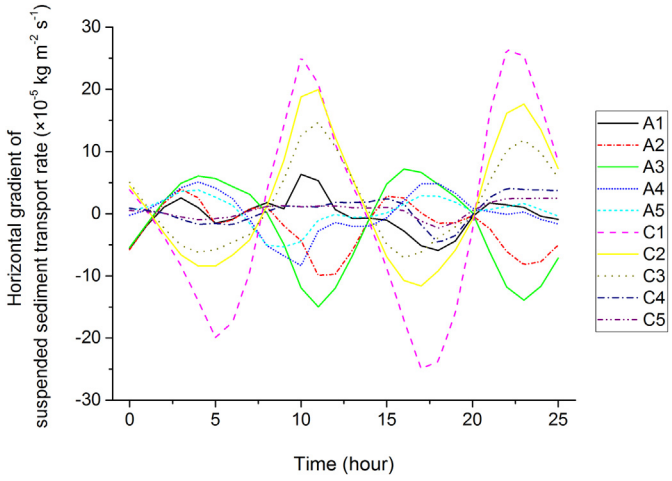

Fig. 10. Time series of horizontal gradient in suspended sediment transport rate at the box boundaries, estimated from the MIKE21 model outputs. A1, A2, A3, C1, C2, C3 are the gradient for southward sediment transport. A4, A5, C4, C5 are the gradient for eastward sediment transport.

a box model with 10^1 km space scale is appropriate, but 10^2 km may not be suitable.

5.3. Application of the box model to accretion/erosion analysis

According to the data collected at Datong (Fig. 1a), the suspended sediment discharge from the Changjiang to the sea has declined significantly since 1980, a pattern linked to sediment starvation caused by human activity and climate change (Gao and Wang, 2008). Based on numerical modeling, Gao (2007) concluded that continuous erosion of the entire Changjiang submarine delta will occur if sediment discharge declines to < 300 Mt yr^{-1}. It is worth noting that the suspended sediment discharge of Changjiang has decreased to 145 Mt yr^{-1} (measured between 2003 and 2012; Yang et al., 2015). This decrease of sediment load has been reported to influence accretion and erosion patterns of the Changjiang subaqueous delta (Yang et al., 2002; Yang et al., 2003), and cause sediment reworking (Gao et al., 2017).

Advection-induced and resuspension-induced SSCs derived from our model, together with the bed-level change measured by *in situ* observations, can help reveal the status of accretion/erosion of the Changjiang subaqueous delta. Fig. 8b shows the periods when either erosion or accretion occurred. For instance, erosion and resuspension processes dominated when the value of C_{re} (blue triangle line) was positive, whereas settling processes dominated when it became negative. During a tidal cycle, the accretion-dominated period was longer than that for erosion and sediment resuspension. However, the bed-level changes in Fig. 8c reveal that the height of the ADV above the bed increased over a short period of time but did not return to its original level, despite the duration of the depositional period being longer than the erosion–resuspension phase. This can be interpreted by the rapid increase in shear stress that caused intense bed erosion. After erosion started, the suspended sediment settled slowly but the amount of settling sediment did not completely compensate the sediment lost due to erosion (Fig. 8c). Therefore, net erosion became a normal state in the study area during the summer season.

Our study area was located near the front of the Changjiang subaqueous delta, where the accretion/erosion pattern is sensitive to the Changjiang sediment discharge. Because of the sediment trapping effect of the upstream Three Gorges Dam, the seabed in our study area had already changed from accretion to erosion. Bed erosion rate here reached up to 15 to 25 cm yr^{-1} from 2004 to 2007 (Yang et al., 2011). With further reduction of the river sediment discharge since 2013, the erosion process has become more intensive (Li et al., 2015). Morphodynamic research of the subaqueous delta was conducted focusing on different aspects, including sediment supply (Du et al., 2016; Li et al., 2007; Luan et al., 2016), bathymetric data (Li et al., 2007; Yang et al., 2011; Zhu et al., 2016), grain size distributions (Yang et al., 2018), numerical model simulation (Luan et al., 2017; Zhu et al., 2016) and isotope dating (Wang et al., 2010; Gao et al., 2011). The evidence from these studies shows that erosion-dominated area increased gradually over the entire subaqueous delta.

A general erosion and accretion pattern of the Changjiang subaqueous delta in the past is that there was accretion in the flood season (summer) but erosion in the dry season (winter) (Liu et al., 2007; Shen et al., 1995; Wan et al., 2006). These studies represent the results of annual averages or multi-year averages. However, bed level changes and the corresponding hydrodynamic conditions in our study showed that the front area of the subaqueous delta presented net erosion during a tidal cycle in the flood seasons, when the river sediment discharge accounted for approximately 80% of the annual sediment load (Dai et al., 2008) and would cause accretion. If the parameters that caused erosion in winter remain unchanged, and net erosion occurs during summer, it is reasonable to conclude that the accretion/erosion pattern of the Changjiang subaqueous delta in the flood season might have been shifted from accretion to erosion. Thus, erosion became the dominated process in both flood and dry seasons. This significant system regime shift supports the observation that erosion was intensified here.

Advection- and resuspension-induced SSCs derived by the box model and the bed-level changes measured can improve our understanding of the accretion/erosion mechanism. Maximum sediment transport rates at station B were the largest of the three stations (Fig. 7) and, as discussed above, sediment accumulation at this station was insufficient to replace the loss by erosion over a tidal cycle. This might be a micro-scale mechanism that causes erosion in the Changjiang

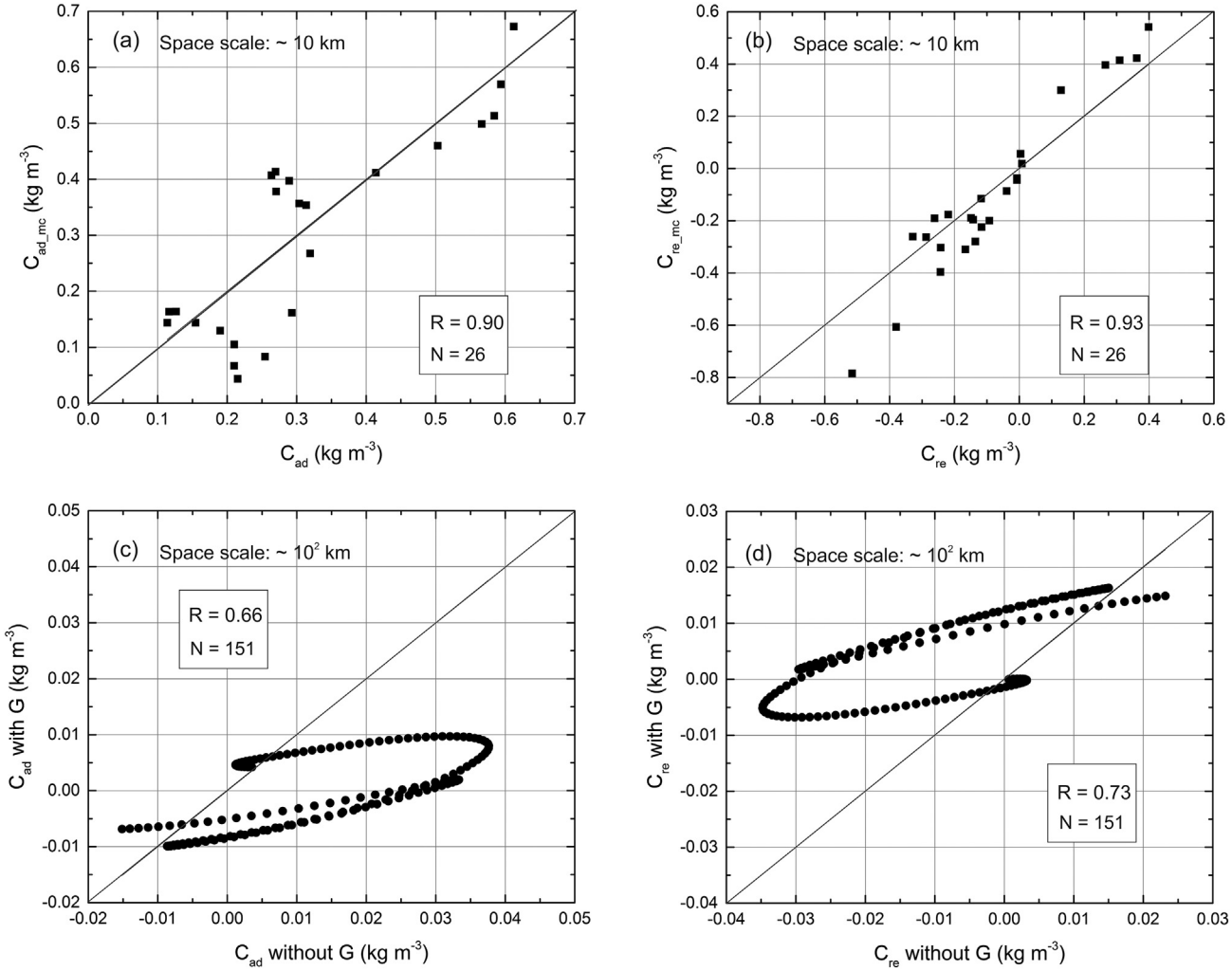
(a) Space scale: ~ 10 km
R = 0.90
N = 26
C_{ad_mc} (kg m^{-3})
C_{ad} (kg m^{-3})
(b) Space scale: ~ 10 km
R = 0.93
N = 26
C_{re_mc} (kg m^{-3})
C_{re} (kg m^{-3})
(c) Space scale: ~ 10^2 km
R = 0.66
N = 151
C_{ad} with G (kg m^{-3})
C_{ad} without G (kg m^{-3})
(d) Space scale: ~ 10^2 km
R = 0.73
N = 151
C_{re} with G (kg m^{-3})
C_{re} without G (kg m^{-3})

Fig. 11. Comparison of original box model (space scale: ~10 km) results and MIKE21 numerical-model-corrected box model results for (a) advection-induced SSC (C_{ad}), and (b) resuspension-induced SSC (C_{re}). Comparison of results analyzed by the MIKE21 numerical model in a large space scale (~10^2 km) with and without the gradient in suspended sediment transport (G; kg m^{-2} s^{-1}) for (c) advection-induced SSC, and (d) resuspension-induced SSC. Absolute errors for (a), (b), (c), and (d) are 0.014 kg m^{-3} (95% confidence interval: −0.033–0.061 kg m^{-3}), −0.014 kg m^{-3} (95% confidence interval: −0.061–0.033 kg m^{-3}), −0.014 kg m^{-3} (95% confidence interval: −0.016 to −0.012 kg m^{-3}), and 0.014 kg m^{-3} (95% confidence interval: 0.012–0.016 kg m^{-3}). Lines denote the one-to-one (y = x) relationship.

subaqueous delta: sediment is being eroded under strong hydrodynamic forcing and advective transport cannot supply sufficient SSC to compensate the loss. Local environments that can cause sediment resuspension (streamflow, tidal currents, waves and estuarine circulation) remain dynamic, but decrease in sediment discharge of Changjiang may have weakened the advective transport in the subaqueous delta. Therefore, changes in intensity of advection and resuspension processes represent a sediment dynamic mechanism underlying the observed morphological changes.

Indeed, *in situ* tidal cycle measurements from the limited study stations cannot reveal the long-term status of the Changjiang subaqueous delta. However, because of the drastic reduction of river sediment discharge, the morphodynamic condition of the Changjiang subaqueous delta had changed into an opposite status. In response to such a regime shift, the box model provides a tool for estimating the resuspension component from SSC observations. This in turn can help identify the local accretion/erosion pattern. Such model-derived resuspension data are valuable for those attempting to evaluate the processes of erosion and accretion on subaqueous deltas.

6. Conclusions

We developed a box model to separate the time series of depth-averaged SSC measurements into their respective advection and resuspension components. This was achieved by estimating advective suspended-sediment transport across the boundaries of a hypothetical box that incorporates current velocity and SSC data obtained from ADCP and OBS (or CTD equipped with a turbidity probe) measurements, respectively. Validation of the methodology was performed by considering the variation of the cumulative bed-level change, which agrees with the changes in SSCs decoupled by the model. The decoupled SSCs indicate that sediment resuspension and advection are both important to suspended sediment transport; thus, suspended sediment is frequently exchanged between the water and the seabed. Horizontal gradient of sediment transport rate at the boundaries of the box model was proved to have relatively small influence on the box model results.

In addition to differentiating the advection and resuspension signals, our box model method can also be used to estimate sediment deposition and transport flux by incorporating marginal stations. In this case, however, additional factors need to be considered, such as the discharge of riverine sediment that can affect sediment transport in

specific areas. Sediment transport rates and cumulative bed-level changes at the center of the box, where the water depth is < 15 m, may provide an indication to explore the accretion/erosion in the Changjiang subaqueous delta. Results showed that the declination of advection sediment supply and the intense resuspension process might be the factors that influence the estuary development.

We used the model-derived resuspension SSC component in conjunction with the ADV Reynolds flux method to estimate settling velocities. Our results show that settling velocity over much of the observation period varied within the range 0.04–6.66 mm s^{-1}, with a mean value of 1.43 mm s^{-1}. However, when suspended sediments changed from settling to resuspension or vice versa, we observed an order-of-magnitude increase in settling velocity, which indicated the occurrence of "intense settling events" during transitional phases.

Acknowledgements

This study was supported by the National Natural Science Foundation of China (41625021, 41376068, 41476004). We thank Tang JP, Chen DZ, Lu HH, Cheng GL, Xiong JL, Ji CC, Cai TL, Chen RZ, Yang D, Xue CF and Chao HJ for their assistance in the field work and laboratory measurements. Finally, we wish to thank the three anonymous reviewers who helped to greatly improve the manuscript.

Appendix A

A calibrated numerical model established by Xing et al. (2012) was used to simulate the hydrodynamics and SSC patterns in the Changjiang Estuary. The simulation period was from 12:00 on June 28 to 12:00 on July 4, 2016, with an output interval of 10 min. Excepting the wind and wave parameters that were replaced by the measured data, the Manning coefficient, critical shear stress of erosion and settling, and other parameters specified in the MIKE21 hydrodynamic and mud transport modules were derived from the model of Xing et al. (2012). Simulation results were validated against observational data collected at each station between 9:00 on July 2 to 10:00 on July 3, 2016 (Fig. A1). Simulated values for water elevation, water speed and direction, and SSC agree well with observed values and thus indicate that the model output is applicable to this study

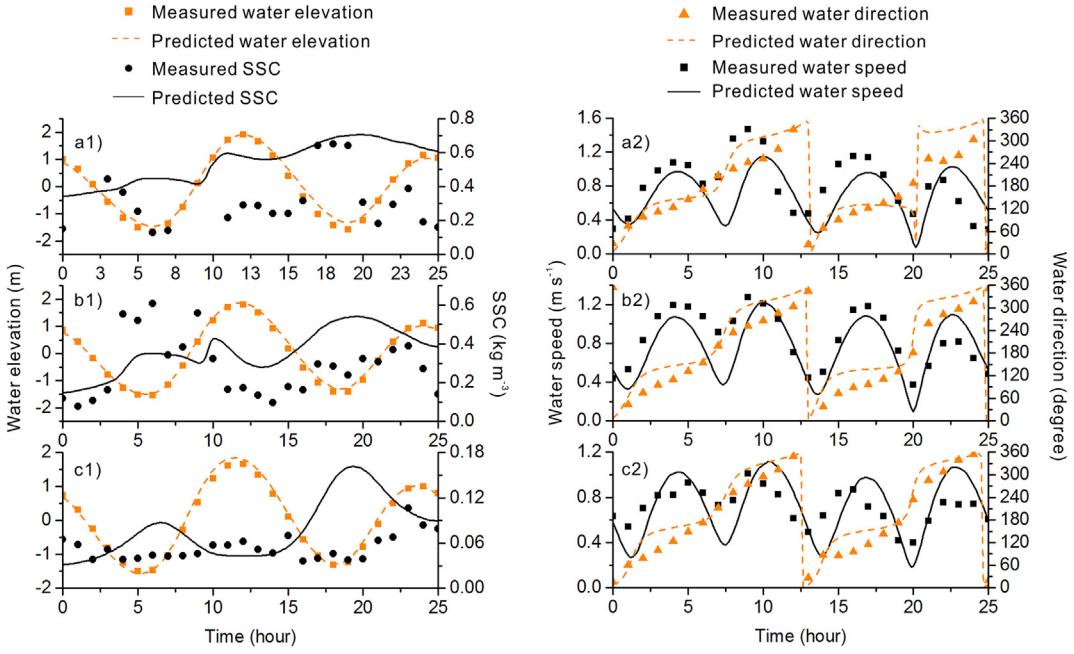

Fig. A1. Relationships between observed and simulated data (water level, SSC, current speed and direction), at stations A (a1, a2), B (b1, b2), and C (c1, c2) from 9:00 on 2 July to 10:00 on 3 July, 2016.

References

Bass, S.J., Aldridge, J.N., Mccave, I.N., Vincent, C.E., 2002. Phase relationships between fine sediment suspensions and tidal currents in coastal seas. J. Geophys. Res. Oceans 107 (10-11-10-14).

Cartwright, G.M., Friedrichs, C.T., Smith, S.J., 2013. A test of the ADV-based Reynolds flux method for in situ estimation of sediment settling velocity in a muddy estuary. Geo-Mar. Lett. 33, 477–484.

Cloern, J.E., Powell, T.M., Huzzey, L.M., 1989. Spatial and temporal variability in South San Francisco Bay (USA). II. Temporal changes in salinity, suspended sediments, and phytoplankton biomass and productivity over tidal time scales. Estuar. Coast. Shelf Sci. 28, 599–613.

Cudaback, C.N., Jay, D.A., 2001. Tidal asymmetry in an estuarine pycnocline: 2. Transport. J. Geophys. Res. Oceans 106, 2639–2652.

Dai, S.B., Lu, X.X., Yang, S.L., Cai, A.M., 2008. A preliminary estimate of human and natural contributions to the decline in sediment flux from the Yangtze River to the East China Sea. Quat. Int. 186, 43–54.

Du, J.L., Yang, S.L., Feng, H., 2016. Recent human impacts on the morphological evolution of the Yangtze River delta foreland: a review and new perspectives. Estuar. Coast. Shelf Sci. 181, 160–169.

Dyer, K.R., 1986. Coastal and Estuarine Sediment Dynamics. John Wiley & Sons Ltd (172p).

Dyer, K.R., 1997. Estuaries-Physical Introduction, second ed. John Wiley and Sons, Chichester (195p).

Friedrichs, C.T., Cartwright, G.M., Dickhudt, P.J., 2008. Quantifying benthic exchange of fine sediment via continuous, noninvasive measurements of settling velocity and bed erodibility. Oceanography 21, 168–172.

Fugate, D.C., Friedrichs, C.T., 2002. Determining concentration and fall velocity of estuarine particle populations using ADV, OBS and LISST. Cont. Shelf Res. 22, 1867–1886.

Gao, S., 2007. Modeling the growth limit of the Changjiang Delta. Geomorphology 85, 225–236.

Gao, S., Wang, Y.P., 2008. Changes in material fluxes from the Changjiang River and their implications on the adjoining continental shelf ecosystem. Cont. Shelf Res. 28, 1490–1500.

Gao, S., Wang, Y.P., Gao, J.H., 2011. Sediment retention at the Changjiang sub-aqueous delta over a 57 year period, in response to catchment changes. Estuar. Coast. Shelf Sci. 95, 29–38.

Gao, J.H., Jia, J., Sheng, H., Yu, R., Li, G.C., Wang, Y.P., Yang, Y., Zhao, Y., Li, J., Bai, F., 2017. Variations in the transport, distribution, and budget of ^{210}Pb in sediment over the estuarine and inner shelf areas of the East China Sea due to Changjiang catchment

changes. J. Geophys. Res. 122, 235–247.
Hamblin, P.F., 1989. Observations and model of sediment transport near the turbidity maximum of the upper Saint Lawrence estuary. J. Geophys. Res. Atmos. 941, 14419–14428.
Helfrich, K.R., 1995. Time-dependent two-layer hydraulic exchange flows. J. Phys. Oceanogr. 25, 359–373.
Hill, D.C., Jones, S.E., Prandle, D., 2003. Derivation of sediment resuspension rates from acoustic backscatter time-series in tidal waters. Cont. Shelf Res. 23, 19–40.
Hout, C.M.V.D., Witbaard, R., Bergman, M.J.N., Duineveld, G.C.A., Rozemeijer, M.J.C., Gerkema, T., 2017. The dynamics of suspended particulate matter (SPM) and chlorophyll-*a* from intratidal to annual time scales in a coastal turbidity maximum. J. Sea Res. 127, 105–118.
Jago, C.F., Jones, S.E., Sykes, P., Rippeth, T., 2006. Temporal variation of suspended particulate matter and turbulence in a high energy, tide-stirred, coastal sea: relative contributions of resuspension and disaggregation. Cont. Shelf Res. 26, 2019–2028.
Jay, D.A., Talke, S.A., Hudson, A., Twardowski, M., 2015. Chapter 2 - estuarine turbidity maxima revisited: instrumental approaches, remote sensing, modeling studies, and new directions. Dev. Sedimentol. 68, 49–109.
Kalnejais, L.H., Martin, W.R., Signell, R.P., Bothner, M.H., 2007. Role of sediment resuspension in the remobilization of particulate-phase metals from coastal sediments. Environ. Sci. Technol. 41, 2282–2288.
Kawanisi, K., Shiozaki, R., 2008. Turbulent effects on the settling velocity of suspended sediment. J. Hydraul. Eng. 134, 261–266.
Krivtsov, V., Gascoigne, J., Jones, S., 2008. Harmonic analysis of suspended particulate matter in the Menai Strait (UK). Ecol. Model. 212, 53–67.
Li, J., Zhang, C., 1998. Sediment resuspension and implications for turbidity maximum in the Changjiang Estuary. Mar. Geol. 148, 117–124.
Li, P., Yang, S., Dai, S., Zhang, W., 2007. Accretion/erosion of the subaqueous delta at the Yangtze Estuary in recent 10 years. Acta Geograph. Sin. 62, 707–716.
Li, B., Yan, X.X., He, Z.F., Chen, Y., Zhang, J.H., 2015. Impacts of the Three Gorges Dam on the bathymetric evolution of the Yangtze River Estuary. Chin. Sci. Bull. 18, 1735–1744 (in Chinese with English abstract).
Li, X., Zhu, J., Yuan, R., Qiu, C., Wu, H., 2016. Sediment trapping in the Changjiang Estuary: observations in the North Passage over a spring-neap tidal cycle. Estuar. Coast. Shelf Sci. 177, 8–19.
Liu, H., He, Q., Wang, Y.Y., Meng, L., 2007. Temporal and spatial characteristics of surface sediment grain-size distribution in Changjiang Estuary. Acta Sedimentol. Sin. 25, 445–455.
Luan, H.L., Ding, P.X., Wang, Z.B., Ge, J.Z., Yang, S.L., 2016. Decadal morphological evolution of the Yangtze Estuary in response to river input changes and estuarine engineering projects. Geomorphology 265, 12–23.
Luan, H.L., Ding, P.X., Wang, Z.B., Ge, J.Z., 2017. Process-based morphodynamic modeling of the Yangtze Estuary at a decadal timescale: controls on estuarine evolution and future trends. Geomorphology 290, 347–364.
Maa, P.Y., Kwon, J.I., 2007. Using ADV for cohesive sediment settling velocity measurements. Estuar. Coast. Shelf Sci. 73, 351–354.
Mitchell, S.B., Green, M.O., MacDonald, I.T., Pritchard, M., 2017. Field studies of estuarine turbidity under different freshwater flow conditions, Kaipara River, New Zealand. Estuar. Coast. Shelf Sci. 198, 542–554.
Salehi, M., Strom, K., 2012. Measurement of critical shear stress for mud mixtures in the San Jacinto estuary under different wave and current combinations. Cont. Shelf Res. 47, 78–92.
Schoellhamer, D.H., 1995. Sediment resuspension mechanisms in Old Tampa Bay, Florida. Estuar. Coast. Shelf Sci. 40, 603–620.
Shao, Y.Y., Yan, Y., Maa, P.Y., 2010. In situ measurements of settling velocity near Baimao Shoal in Changjiang Estuary. J. Hydraul. Eng. 137, 372–380.
Shen, H., Li, J., Jin, Y., 1995. Evolution and regulation of flood channels in estuaries. Oceanologia Et Limnologia Sinica 26, 83–89.
Shen, H., Mao, Z., Zhu, J., 2003. Saltwater Intrusion in the Changjiang Estuary. China Ocean Press, Beijing (175p, in Chinese with English abstract).
Shi, Z., Zhou, H.J., Eittreim, S.L., Winterwerp, J.C., 2003. Settling velocities of fine suspended particles in the Changjiang Estuary, China. J. Asian Earth Sci. 22, 245–251.
Stacey, M.T., Burau, J.R., Monismith, S.G., 2001. Creation of residual flows in a partially stratified estuary. J. Geophys. Res. Oceans 106, 17013–17037.
Sternberg, R., Larsen, L., Miao, Y., 1985. Tidally driven sediment transport on the East China Sea continental shelf. Cont. Shelf Res. 4, 105–120.
Su, J.L., Wang, K., 1986. The suspended sediment balance in Changjiang Estuary. Estuar. Coast. Shelf Sci. 23, 81–98.
Thorne, P.D., Hanes, D.M., 2002. A review of acoustic measurement of small-scale sediment processes. Cont. Shelf Res. 22, 603–632.
Uncles, R.J., 2002. Estuarine physical processes research: some recent studies and progress. Estuar. Coast. Shelf Sci. 55, 829–856.
Valipour, R., Boegman, L., Bouffard, D., Rao, Y.R., 2017. Sediment resuspension mechanisms and their contributions to high-turbidity events in a large lake. Limnol. Oceanogr. 62, 1–21.
Voulgaris, G., Meyers, S.T., 2004. Temporal variability of hydrodynamics, sediment concentration and sediment settling velocity in a tidal creek. Cont. Shelf Res. 24, 1659–1683.
Wan, X.N., Li, J.F., Shen, H.T., 2006. Distribution and diffusion of suspended sediment in the offshore area of Changjiang estuary,China. Geogr. Res. 25, 294–302.
Wang, A., Pan, S., Zhang, Y., Liu, Z., 2010. Modern sedimentation rate of the submarine delta of the Changjiang River. Mar. Geol. Quat. Geol. 30, 1–6.
Wang, Y.P., Voulgaris, G., Li, Y., Yang, Y., Gao, J., Chen, J., Gao, S., 2013. Sediment resuspension, flocculation, and settling in a macrotidal estuary. J. Geophys. Res. Oceans 118, 5591–5608.
Weeks, A.R., Simpson, J.H., Bowers, D., 1993. The relationship between suspended particulate matter and tidal processes in the Irish Sea. Cont. Shelf Res. 13, 1325–1334.
Whitehouse, R., Soulsby, R., Roberts, W., Mitchener, H., 2000. Dynamics of Estuarine Muds. Thomas Telford Ltd (210p).
Xie, D., Pan, C., Wu, X., Gao, S., Wang, Z., 2017. The variations of sediment transport patterns in the outer Changjiang Estuary and Hangzhou Bay over the last 30 years. J. Geophys. Res. 122, 2999–3020.
Xing, F., Wang, Y.P., Wang, H.V., 2012. Tidal hydrodynamics and fine-grained sediment transport on the radial sand ridge system in the southern Yellow Sea. Mar. Geol. 291–294, 192–210.
Yang, S.L., Ding, P.X., Chen, S.L., 2001. Changes in progradation rate of the tidal flats at the mouth of the Changjiang (Yangtze) River, China. Geomorphology 38, 167–180.
Yang, S.L., Zhao, Q.Y., Belkin, I.M., 2002. Temporal variation in the sediment load of the Yangtze River and the influences of human activities. J. Hydrol. 263, 56–71.
Yang, S.L., Belkin, I., Belkina, A., Zhao, Q., Zhu, J., Ding, P., 2003. Delta response to decline in sediment supply from the Yangtze River: evidence of the recent four decades and expectations for the next half-century. Estuar. Coast. Shelf Sci. 57, 689–699.
Yang, S.L., Li, H., Ysebaert, T., Bouma, T.J., Zhang, W.X., Wang, Y.Y., Li, P., Li, M., Ding, P.X., 2008. Spatial and temporal variations in sediment grain size in tidal wetlands, Yangtze Delta: on the role of physical and biotic controls. Estuar. Coast. Shelf Sci. 77, 657–671.
Yang, S.L., Milliman, J.D., Li, P., Xu, K., 2011. 50,000 dams later: erosion of the Yangtze River and its delta. Glob. Planet. Chang. 75, 14–20.
Yang, S.L., Xu, K., Milliman, J., Yang, H., Wu, C., 2015. Decline of Yangtze River water and sediment discharge: impact from natural and anthropogenic changes. Sci. Rep. 5, 1–14.
Yang, H.F., Yang, S.L., Meng, Y., Xu, K.H., Luo, X.X., Wu, C.S., Shi, B.W., 2018. Recent coarsening of sediments on the southern Yangtze subaqueous delta front: a response to river damming. Cont. Shelf Res. 155, 45–51.
Zhu, L., He, Q., Shen, J., Wang, Y., 2016. The influence of human activities on morphodynamics and alteration of sediment source and sink in the Changjiang Estuary. Geomorphology 273, 52–62.